1) CSF clearance in Alzheimer Disease measured with dynamic PET

2) Running title: Impaired CSF clearance in Alzheimer

3) Mony J. de Leon[1][*][+], Yi Li[1][*], Nobuyuki Okamura[2], Wai H. Tsui[1] , Les A. Saint-Louis[3], Lidia Glodzik[1][,4], Ricardo S. Osorio[1], Juan Fortea[5], Tracy Butler[1], Elizabeth Pirraglia[1], Silvia Fossati[1][,6], Hee-Jin Kim[1][,7], Roxana O. Carare[8], Maiken Nedergaard[9], Helene Benveniste[10], and Henry Rusinek[4][*]

4) Affiliations: New York University Center for Brain Health, Departments of [1]Psychiatry, [6]Neurology, and [4]Radiology, New York.

[2]Department of Pharmacology, Tohoku University School of Medicine, Tohoku, Japan.

[3]Manhattan Diagnostic Radiology, NY NY.

[5]Alzheimer's Disease and Other Cognitive Disorders Unit, Neurology Service, Hospital de la Santa Creu i Sant Pau, Universitat Autónoma de Barcelona, Barcelona, Spain.

[7]Department of Neurology, Konkuk University College of Medicine, Seoul, Korea.

[8]Faculty of Medicine, University of Southampton, Southampton, UK.

[9]Center for Translational Neuromedicine, University of Rochester Medical Center, Rochester, NY. 14642, USA and Center for Basic and Translational Neuroscience, University of Copenhagen, Copenhagen, Denmark.

[10]Department of Anesthesiology, Stony Brook University, Stony Brook, NY.

5) *contributed equally to the paper

6) +corresponding author: Dr. Mony de Leon, New York University, Department of Psychiatry, Center for Brain Health, 145 East 32 Street New York, NY 10016, .T) 212 2635805, F) 212 263 3270, mony.deleon@nyumc.org

7) Same as above

8) 4,977 words

ABSTRACT

Evidence supporting the hypothesis that reduced cerebrospinal fluid (CSF) clearance is involved in the pathophysiology of Alzheimer's disease (AD) comes from primarily from rodent models. However, unlike rodents where predominant extra-cranial CSF egress is via olfactory nerves traversing the cribriform plate, human CSF clearance pathways are not well characterized. Using dynamic Positron Emission Tomography (PET) with ^{18}F-THK5117 a tracer for tau pathology, the ventricular CSF time activity was used as a biomarker for CSF clearance. We tested three hypotheses: 1. Extra-cranial CSF is detected at the superior turbinates; 2. CSF clearance is reduced in AD; and 3. CSF clearance is inversely associated with amyloid deposition. **Methods.** 15 subjects, 8 with AD and 7 normal control volunteers were examined with ^{18}F-THK5117. 10 subjects additionally received ^{11}C-PiB PET scans and 8 were PiB positive. Ventricular time activity curves (TAC) of ^{18}F-THK5117 were used to identify highly correlated TAC from extra-cranial voxels. **Results.** For all subjects, the greatest density of CSF positive extra-cranial voxels was in the nasal turbinates. Tracer concentration analyses validated the superior nasal turbinate CSF signal intensity. AD patients showed ventricular tracer clearance reduced by 23% and 66% fewer superior turbinate CSF egress sites. Ventricular CSF clearance was inversely associated with amyloid deposition. **Conclusions.** The human nasal turbinate is part of the CSF clearance system. Lateral ventricle and superior nasal turbinates CSF clearance abnormalities are found in AD. Ventricular CSF clearance reductions are associated with increased brain amyloid depositions.

These data suggest that PET measured CSF clearance is a biomarker of potential interest in AD and other neurodegenerative diseases.

INTRODUCTION

Impairments in CSF turnover have been suspected for many years in the etiology of Alzheimer's disease (AD) and propagation of amyloid-β (Aβ) lesions *(1-4)*. However, there are no non-invasive imaging tools to evaluate CSF clearance.

Impaired CSF clearance, is observed in mouse aging *(5)* and AD *(6)* models. In rodents and other mammals, CSF is primarily cleared along olfactory nerves that traverse the cribriform plate, draining into lymphatic vessels in the nasal mucosa *(7-10)*. Rodent CSF clearance is rapid as radio- labeled albumin *(11)*, Indian ink*(7)* and paramagnetic contrast*(10)* injected into the CSF reach the turbinates within minutes. Much less is known about human CSF clearance anatomy. Arachnoid granulations, arguably considered important human CSF egress sites*(12)*, are not found in the rodent. The only evidence for a human nasal turbinate CSF efflux pathway comes from post mortem studies *(13,14)*.

Low molecular weight radiotracers enter and egress the CSF through the choroid plexus and perivascular drainage*(12)*, yet CSF time activity curves (TAC) have not been explored in the PET literature. Using in vivo dynamic PET with ^{18}F-THK5117 and ^{11}C-PiB tracers in healthy elderly and AD subjects, ventricular CSF TAC were used to confirm three hypotheses: 1. CSF is cleared via the superior nasal turbinates; 2. CSF clearance is reduced in AD; and 3. the magnitude of Aβ binding is inversely associated with the CSF clearance.

MATERIALS AND METHODS

Participants and clinical assessments

With ethics committee approval, written informed consent was obtained from 15 participants or their legal care takers. 8 probable AD patients were recruited from the memory clinic of Tohoku University Hospital and 7 healthy normal (NL) volunteer controls were recruited from the community (Table 1). All subjects were diagnosed at a consensus conference and the diagnosis of AD was made in accordance with the National Institute of Neurological and Communicative Disorders and Stroke/AD and Related Disorders Association criteria *(15)*. All participants received a high resolution T1 weighted MRI and PET examination with the ^{18}F-THK5117 tracer. Ten of these subjects, 5 NL and 5 AD also received an ^{11}C-PiB PET scan.

Image acquisition and processing

Dynamic PET acquisition:

The PET radiotracers were administered in two imaging sessions within 2 weeks. The radiotracers included: ^{18}F-THK5117, an 2-arylquinoline derivative validated for neurofibrillary pathology *(16)* and Pittsburgh compound B (^{11}C-PiB), an analog of thioflavin-T validated for brain beta-amyloid (Aβ) plaques *(17)*. Both tracers were prepared at the Cyclotron and Radioisotope Center of Tohoku University,

both have low molecular weight (<328g/mole) and both freely cross the blood-brain barrier *(18,16)*. 185 mBq of ^{18}F-THK5117 and 296 mBq of ^{11}C-PiB were administered by IV bolus injection. Dynamic PET data were acquired axially along the cantho-meatal plane in list mode continuously up to 90 min using a SET-3000 G/X PET scanner (Shimadzu, Kyoto, Japan *(19)*). Supplemental File 1 lists the timing of the reconstructed PET image frames. The scanner is equipped with high energy resolution germanium oxyorthosilicate scintillators that provide 4.5 mm (transverse) and 5.4 mm (axial) spatial resolutions (full width at half maximum, at 10 cm off axis). Attenuation correction was based on transmission image from a rotating 137-Cs point source. The field of view (FOV) superiorly encompassed the skull and inferiorly the foramen magnum and maxilla.

MRI acquisition*:*

Each subject received an MRI on a GE SIGNA 1.5 T magnet (General Electric, Milwaukee, WI, USA).The protocol included a T1-weighted SPGR gradient echo axial sequence with parameters: echo time/repetition time, 2.4/ 22 ms; flip angle 20°; acquisition matrix 256×256x110; 1 excitation; axial field of view 22 cm, bandwidth 122Hz/px, 0.86 x 0.86 x 1.0 voxel size. In all cases, the MRI FOV covered the PET FOV.

PET Image Workflow:

PET data were reconstructed to a 128 x 128 x 79 matrix of 2 x 2 x 2.6 mm voxels. After decay correction and standardized uptake value (SUV) normalization, each

dynamic PET frame was coregistered with the corresponding T1 weighted MRI using Statistical Parametric Mapping (SPM 12) software (www.fil.ion.ucl.ac.uk/spm). PET images were sampled in their original space and partial volume corrected using a modified one tissue model *(20)*

MRI Regional Segmentation:

To explore CSF egress, an extra-cranial shell region of interest (ROI) was defined on MRI. The shell included scalp, bone and soft tissues (muscle, nasal turbinates, and globes of the eye) and extended inferiorly to the foramen magnum and maxilla. It excluded brain, subarachnoid CSF, and air (see Fig. 1). The following shell ROIs were drawn on the MRI blind to the PET data:

1. The superior nasal turbinates were sampled at a distance 5.2mm (2 voxels) inferior to the frontal lobe in order to minimize partial volume effects from brain. The anterior boundary was at the crista galli. The ROI dimensions were 18 mm anterior-posterior (A-P), 14mm left-right (L-R), and 10mm cranio-caudal.

2. The middle nasal turbinates were sampled inferior to the superior turbinate with the following ROI dimensions: 34mm A-P, 16mm L-R and 18mm cranio-caudal.

3. The globes of the eyes and lateral pterygoid muscle were sampled bilaterally and both ROIs were 12mm A-P, 12 L-R, and 6mm cranio-caudal.

The MRI brain was segmented into lateral ventricle, neocortical gray and white matter, and cerebellar hemisphere gray matter using Free-Surfer (V. 5.1,

http://surfer.nmr.mgh.harvard.edu). The ventricular CSF ROI was shrunk by 2 voxels (5.2mm) to minimize partial volume contamination from brain tissue (see Fig. 1D). Image-derived arterial blood tracer concentrations were sampled from the internal carotid artery *(21)* and venous blood sampled at the junction of the superior sagittal and transverse sinus.

Mapping CSF clearance in the shell:

CSF positive voxels were identified in each subject using a "seeding" procedure similar to one used to identify neural networks in resting fMRI*(22)*. The TAC of every shell voxel was correlated (Pearson Product r) with the TAC from the ventricular CSF (see Supplemental File 2). Voxels whose correlations were r >.95 were considered potentially CSF positive and further tested for tracer concentrations.

Tracer concentration estimations and CSF validation*:*

Voxel tracer concentrations were derived from the SUV data normalized by the corresponding cerebellar gray matter time frames and were examined as area under the curve (AUC) and as the rate of change. For THK5117, the 35-80min time period was selected because blood concentrations were consistently low and confirmed in another study *(23)*. The CSF validation for each shell region was determined by contrasting the average tracer concentrations of the positive shell voxels, against tracer concentrations from ventricular CSF, blood, and brain.

Measures of tracer binding:

Conventional time frames used to estimate tracer binding were: 50-80min for ^{18}F-THK5117 and 50-70min for ^{11}C-PiB. Both measures were normalized by their respective cerebellar gray matter SUV to form the SUV ratio (SUVR). SUVR values $\geq$ 1.5 defined positive voxels *(24)*.

Statistical analysis

Correlations were examined with Spearman tests and partial correlations using Quade's "index of matched correlation"*(25)*. Between group contrasts were made with the Mann-Whitney U. Within subject anatomical specificity tests were examined with the related samples Wilcoxon Signed Rank Tests. The Holm-Bonferroni method for multiple comparisons was used for p value adjustment *(26)*. All tests were two-sided and statistical significance was set at p<.05 when not adjusted for multiple comparisons.

RESULTS

Study 1. Anatomical distribution and validation of nasal cavity CSF.

　　Nasal cavity CSF: Across all subjects, the TAC correlation analysis showed a three-fold greater percentage of CSF positive extra-cranial voxels (red) in the nasal cavity (yellow) than in the rest of the total shell in blue, (Fig. 2).

　　ROI Analyses: All subjects had CSF positive voxels in the superior turbinate ROI (Fig. 3). Among the extra-cranial ROIs, the superior turbinate ROI

had the greatest tracer concentration. Both superior and middle turbinate ROIs show >23% CSF positive voxels density, while the globe of the eye, pterygoid muscle, and total shell showed <5% (Table 2). After partial volume correction the superior turbinate concentration remained the greater (Supplemental File 3). Using ^{11}C-cocaine, a PET tracer with little neocortical uptake, rapid clearance, and no nasal turbinate binding, a high density of CSF positive nasal turbinate voxels was confirmed in 4 normal subjects (Supplemental File 4). A video depicts for one NL the extra-cranial CSF transit over 9 min (Supplemental File 5).

CSF validation of positive shell voxels: The CSF origin of the positive superior turbinate voxels was supported by tracer concentration analyses, n=15. The average tracer concentration of the positive turbinate voxels (1.27+/- 0.25), did not differ from the ventricular CSF (1.27+/- 0.34, p>.05). However, positive superior turbinate voxels had significantly lower tracer concentrations than brain (2.69 +/-0.40, W=3.41, p<0.01) and were higher than blood (arterial 0.94 +/- 0.31, W=-2.56, p$\leq$.01, and venous 0.96 +/- 0.22, W=-2.33, p<.05, Fig. 4).

Study 2. CSF clearance in AD

The ventricle $AUC_{35-80min}$ was 23% lower in AD as compared with NL (.53 +/- .08 and .69 +/- .09 respectively, U=7, p=.01). The rate of ventricular CSF clearance was reduced 33% in AD (.29 +/- .08 and .43 +/- .10 respectively, U=4, p<.01, Fig. 5A and 5B). 66% fewer CSF positive superior turbinate voxels were found in AD

vs. NL (39.4 +/- 18.5 vs. 115.1 +/- 71.1, U=7, p=.01, Fig. 5C). The significance of these results was unchanged after partial volume correction.

Study 3. CSF clearance and amyloid positivity.

8 of 10 subjects, including 5 AD and 3 NL were ^{11}C-PiB positive. Both the ventricle $AUC_{35-80min}$ and the rate of ventricular CSF clearance from THK-5117 were inversely correlated with gray matter amyloid binding (rho=.93, p<.01 and rho=.74, p<.05, respectively, Fig. 6). Demonstrating the precision of the ventricle measurement, the THK5117 $AUC_{35-80min}$ and PiB $AUC_{35-80min}$ were highly correlated (rho=.83, p<.01 Supplemental file 6). Compared with THK5117, PiB showed greater binding in the turbinate cavity (THK-5117 SUVR= 58 $\pm$ .12 and PiB SUVR = 1.31 $\pm$ .32, n=10). Therefore, the PiB turbinates were not explored.

Examination of Confounds.

Five potential confounds were examined. First, elevated tau binding in AD would be expected to reduce the available tau tracer to be cleared to CSF. The extent of this effect was estimated by comparing the ventricular $AUC_{35-80min}$ after cerebellar normalization, a reference region without specific binding, with whole brain normalization, which includes all specific and non-specific binding sites (Supplemental File 7). Relative to cerebellar normalization, whole brain normalization reduced the AUC by 28% in normal and 31% in AD. The between group AUC differences went from 30% to 36% and remained significant (U=5, p<.01). This suggests a relatively greater between group tracer clearance effect

than tracer binding effect. Similarly, after statistical adjustment for the total brain binding, the between group ventricle $AUC_{35-80min}$ effect remained significant (F=7.8, p=0.02). Second, partial volume errors for the ventricular and extra-cranial regions were minimized by individually sampling the PET at a 5mm distance or greater from brain. Additional partial volume corrections did not change the region or group contrasts. Third, we examined the effect of the larger AD ventricle (58.3mL +/- 14.1) as compared to normal (32.2mL +/- 11.9, U=50, p<0.01). After adjustment for ventricular volume, the ventricle $AUC_{35-80min}$ and its rate of change remained lower in AD (both F=5.0 p<0.05). Fourth, no ^{18}F-THK5117 binding was observed in the nasal turbinates and there were no between group turbinate binding differences (SUVR-NL= 0.56+/-0.10 and SUVR-AD= 0.62+/-0.06, p>.05). These data rule out contamination from the nasal mucosa. Fifth, we modeled the effects of reduced flow on the $AUC_{10-35min}$ and $AUC_{35-80min}$. The results demonstrate negligible flow effects after 10min thus supporting our conservative 35min start point (Supplemental File 8).

DISCUSSION

Human Nasal Turbinate CSF Egress.

All non-human mammals studied show similar CSF egress pathways that include: choroid plexus, cerebral ventricles, perivascular spaces, and a predominant olfactory nerve drainage site *(27,12,13)*. It is through these pathways that Aβ and other molecules carried in the CSF are removed from brain *(27,28)*. Human egress sites are poorly understood. It is believed that CSF drains via para-neural

pathways and via arachnoid granulations located in brain and spinal cord (a structure not found in the rodent) *(12)*.

Our results using dynamic PET with ^{18}F-THK5117 show that CSF can be detected in the superior nasal turbinates in all subjects. This finding was and replicated using ^{11}C-Cocaine. Our validation study shows that superior turbinate tracer concentrations uniquely differ from other extra-cranial regions, but not from the ventricular CSF concentrations. These results are anatomically consistent with in vivo rodent*(11)* and post mortem human observations *(13,14)* demonstrating a CSF egress pathway through the cribriform plate, as well as the rapid intranasal delivery of macromolecules to the CSF *(29)*.

CSF Egress in AD.

Our results show that ventricular CSF clearance is 23% lower in AD as compared with NL and the number of CSF positive superior turbinate voxels reduced by 66%. Impairments in CSF turnover have been hypothesized for many years in the etiology of AD and propagation of Aβ *(1-4)*. Unfortunately, neither the animal model nor human evidence is well developed. The pioneering human studies by Bateman *(30)* used IV administered [13]C[6]-leucine to reveal the time course of labelled Aβ in LP derived CSF. They demonstrated that Aβ clearance, but not Aβ production, was reduced in AD *(31)*. However, their method does not distinguish between impaired membrane transport of Aβ *(4)* and impaired CSF clearance which carries the Aβ. Sugggesting CSF clearance abnormalities in AD, impaired glymphatic CSF clearance, was recently observed in aged wild type mice *(5)* and

in an AD mouse model *(6)*. The known driving forces behind CSF clearance include: cardiac output, vasocontractility, and CSF production, facilitated by aquaporin-4 function on egress channels *(12)*. Further, environmental factors such as impaired sleep *(32)*, low activity level *(33)*, and brain inflammation *(34)* can adversely affect clearance, and all are affected by aging *(12,35,36)*. However, the cause and chronology of impaired CSF clearance and Aβ pathology is unknown. Imparied CSF clearance could both promote and be a consequence of Aβ pathology. Furthermore, surgical CSF drainage therapy failed to show cognitive benefit in an AD population highlighting the complexity of these relationships *(37)*. Nevertheless, our cross-sectional observation of reduced CSF clearance in AD and of an inverse association between reduced CSF clearance and elevated brain Aβ levels presents the first *in vivo* support for the hypothesis. Longitudinal study is needed to validate the hypothesis and sort out the chronological relationships between reduced CSF clearance and brain Aβ plaques.

Study Limitations.

Our data have several limitations. The correlated timing of the THK5117 tracer delivery from ventricle to extra-cranial sites, the basis of our nasal turbinate CSF detection strategy, could be limited by intermittent obstacles to CSF flow. Perivascular CSF channels in AD brain accumulate Aβ *(9)* and specific and non-specific tracer binding can directly obstruct clearance by binding in clearance sites or by indirectly reducing the concentration available for clearance. We

selected the r>.95 threshold to maintain precision in identifying extra-cranial CSF voxels.

Unlike tau tracer AV1451 *(38)* we found no evidence for THK5117 uptake in choroid plexus. Such uptake would confound the ventricular PET signal. For this reason, PiB which shows binding in the nasal turbinates was not used to estimate turbinate clearance. On the other hand, ^{11}C-cocaine, which does not show cortical or turbinate binding was valuable as a validator. In our study of ventricular CSF clearance, we controlled for the total tissue binding of THK5117 and conclude that the between group clearance effect was largely unchanged. Similarly, we observed that THK5117 and PiB estimates of ventricular CSF clearance were highly correlated within subjects, a finding supportive of the method's precision when sampling the CSF directly.

Our estimates of nasal tracer concentrations are not precise owing to the relatively poor spatial resolution and resultant partial volume errors. Spatial resolution limitations are likely to have affected the tracer concentrations in the sparsely packed turbinate voxels which did not show clearance reductions in AD. Spatial resolution limitations also limited measurement of CSF clearance from the arachnoid granulations. On the other hand, the larger lateral ventricle provided robust CSF tracer concentration estimates and performed well as a clearance biomarker.

For the present, PET provides the only non-invasive strategy for estimating CSF clearance. Recently, Benveniste et al reported using MRI that intrathecal contrast administration in an animal model could be used to image CSF bulk flow *(10)*, but this approach is not feasible in clinical practice. Phase Contrast MRI is the only other non-invasive approach to estimate CSF flow in human. However, it is increasingly recognized that the results are imprecise and of limited clinical utility due to slow CSF velocity rates *(12)*. Overall, despite suboptimal tracers and obvious spatial resolution limitations, we provide the first evidence that dynamic PET yields important insight into CSF clearance. Our results highlight the importance of a ventricle clearance biomarker and suggest exploiting the nasal pathway for the sampling CSF molecules cleared from the brain. Finally, we view our study as a preliminary proof of concept, needing larger sample sizes, test-retest reliability, and longitudinal observations. Future studies will be served by developing comprehensive PET models that consider CSF flow in addition to estimating tracer uptake into tissue.

CONCLUSION

Dynamic PET was used to estimate in humans the CSF clearance in ventricular and extra-cranial regions. As in other mammals, we find the human nasal turbinates are part of the CSF egress system. Ventricular CSF and superior nasal turbinate clearance measures were reduced in AD in comparison to control. Consistent with the clearance hypothesis of AD, ventricular CSF clearance was inversely related to Aβ deposition. PET based CSF clearance measures may be

of interest in the evaluation of the propagation and clearance of Aβ and other abnormal proteins.

ACKNOWLEDGEMENTS

REFERENCES

(1) Hardy J, Selkoe DJ. The Amyloid Hypothesis of Alzheimer's disease: Progress and Problems on the road to Therapeutics. *Science.* 2002;297:353-356.

(2) Silverberg G, Heit G, Huhn S et al. The cerebrospinal fluid production rate is reduced in dementia of the Alzheimer's type. *Neurol.* 2001;57:1763-1766.

(3) Ethell DW. Disruption of cerebrospinal fluid flow through the olfactory system may contribute to Alzheimer's disease pathogenesis. *J Alzheimers Dis.* 2014;41:1021-1030.

(4) Tarasoff-Conway JM, Carare RO, Osorio RS et al. Clearance systems in the brain-implications for Alzheimer disease. *Nat Rev Neurol.* 2015;11:457-470.

(5) Kress BT, Iliff JJ, Xia M et al. Impairment of paravascular clearance pathways in the aging brain. *Ann Neurol.* 2014;76:845-861.

(6) Peng W, Achariyar TM, Li B et al. Suppression of glymphatic fluid transport in a mouse model of Alzheimer's disease. *Neurobiol Dis.* 2016;93:215-225.

(7) Kida S, Pantazis A, Weller RO. CSF drains directly from the subarachnoid space into nasal lymphatics in the rat. Anatomy, histology and immunological significance. *Neuropathol Appl Neurobiol.* 1993;19:480-488.

(8) Weller RO, Djuanda E, Yow HY, Carare RO. Lymphatic drainage of the brain and the pathophysiology of neurological disease. *Acta Neuropathologia.* 2009;117:1-14.

(9) Carare RO, Bernardes-Silva M, Newman TA et al. Solutes, but not cells, drain from the brain parenchyma dextran: flouspheres; cerebral amyloid angiopathy and neuroimmunology. *Neuropathol Appl Neurobiol.* 2008;34:131-144.

(10) Illiff j.j, Lee H, Yu M et al. Brain-wide pathway for waste clearance captured by contrast-enhanced MRI. *J Clin Invest.* 2013;123(3):1299-1309.

(11) Nagra G, Koh L, Zakharov A, Armstrong D, Johnston M. Quantification of cerebrospinal fluid transport across the cribriform plate into lymphatics in rats. *Am J Physiol Regul Integr Comp Physiol.* 2006;291:1383-1389.

(12) Hladky SB, Barrand MA. Mechanisms of fluid movement into, through and out of the brain: evaluation of the evidence. *Fluids Barriers CNS.* 2014;11:11-26.

(13) Johnston M, Zakharov A, Papaiconomou C, Salmasi G, Armstrong D. Evidence of connections between cerebrospinal fluid and nasal lymphatic vessels in humans, non-human primates and other mammalian species. *Cerebrospinal Fluid Res.* 2004;1:2.

(14) Pan WR, Suami H, Corlett RJ, Ashton MW. Lymphatic drainage of the nasal fossae and nasopharynx: Preliminary anatomical and radiological study with clinical implications. *Head Neck.* 2009;31:52-57.

(15) McKhann GM, Knopman DS, Chertkow H et al. The diagnosis of dementia due to Alzheimer's disease: Recommendations from the National Institute on Aging-Alzheimer's Association workgroups on diagnostic guidelines for Alzheimer's disease. *Alzheimers Dement.* 2011;7:263-269.

(16) Okamura N, Furumoto S, Harada R et al. Novel 18F-Labeled Arylquinoline Derivatives for Noninvasive Imaging of Tau Pathology in Alzheimer Disease. *J Nucl Med.* 2013;54:1420-1427.

(17) Klunk WE, Engler H, Nordberg A et al. Imaging brain amyloid in Alzheimer's disease with Pittsburgh Compound-B. *Ann Neurol.* 2004;55:306-319.

(18) Price JC, Klunk WE, Lopresti BJ et al. Kinetic modeling of amyloid binding in humans using PET imaging and Pittsburgh Compound-B. *J Cereb Blood Flow Metab.* 2005;25:1528-1547.

(19) Matsumoto K, Kitamura K, Mizuta T et al. Performance Characteristics of a New 3-Dimensional Continuous-Emission and Spiral-Transmission High-Sensitivity and High-Resolution PET Camera Evaluated with the NEMA NU 2-2001 Standard. *J Nucl Med.* 2006;47:83-90.

(20) Schwarz CG, Senjem ML, Gunter JL et al. Optimizing PiB-PET SUVR change-over-time measurement by a large-scale analysis of longitudinal reliability, plausibility, separability, and correlation with MMSE. *Neuroimage.* 2017;144, Part A:113-127.

(21) Su Y, Blazey TM, Snyder AZ et al. Quantitative Amyloid Imaging Using Image-Derived Arterial Input Function. *PLoS One.* 2015;10(4):e0122920.

(22) Lee MH, Smyser CD, Shimony JS. Resting-State fMRI: A Review of Methods and Clinical Applications. *Am J Neuroradiol.* 2013;34:1866-1872.

(23) Jonasson M, Wall A, Chiotis K et al. Tracer Kinetic Analysis of (S)-18F-THK5117 as a PET Tracer for Assessing Tau Pathology. *J Nucl Med.* 2016;57:574-581.

(24) Li Y, Tsui W, Rusinek H et al. Cortical Laminar Binding of PET Amyloid and Tau Tracers in Alzheimer Disease. *J Nucl Med.* 2015;56:270-273.

(25) Quade D. Rank analysis of covariance. *J Am Stat Assoc.* 1967;62:1187-1200.

(26) Holm S. A Simple Sequentially Rejective Multiple test procedure. *Scandinavian Journal Of Statistics.* 1970;6:65-70.

(27) Pollay M. The function and structure of the cerebrospinal fluid outflow system. *Cerebrospinal Fluid Res.* 2010;7:1-20.

(28) Weller RO, Kida S, Zhang ET. Pathways of fluid drainage from the brain--morphological aspects and immunological significance in rat and man. *Brain Pathol.* 1992;2:277-284.

(29) Lochhead JJ, Wolak DJ, Pizzo ME, Thorne RG. Rapid transport within cerebral perivascular spaces underlies widespread tracer distribution in the brain after intranasal administration. *J Cereb Blood Flow Metab.* 2015;35:371-381.

(30) Bateman RJ, Munsell LY, Morris JC, Swarm R, Yarasheski KE, Holtzman DM. Human amyloid-beta synthesis and clearance rates as measured in cerebrospinal fluid in vivo. *Nat Med.* 2006;12:856-861.

(31) Mawuenyega KG, Sigurdson W, Ovod V et al. Decreased Clearance of CNS Beta-Amyloid in Alzheimer's Disease. *Science.* 2010;330:1774.

(32) Kang JE, Lim MM, Bateman RJ et al. Amyloid-beta dynamics are regulated by orexin and the sleep-wake cycle. *Science.* 2009;326:1005-1007.

(33) Cirrito JR, Yamada KA, Finn MB et al. Synaptic activity regulates interstitial fluid amyloid-beta levels in vivo. *Neuron.* 2005;48:913-922.

(34) Minter MR, Taylor JM, Crack PJ. The contribution of neuroinflammation to amyloid toxicity in Alzheimer's disease. *J Neurochem.* 2016;136:457-474.

(35) Iliff JJ, Wang M, Zeppenfeld DM et al. Cerebral Arterial Pulsation Drives Paravascular CSF Interstitial Fluid Exchange in the Murine Brain. *J Neurosci.* 2013;33(46):18190-18199.

(36) Tolppanen AM, Solomon A, Kulmala J et al. Leisure-time physical activity from mid- to late life, body mass index, and risk of dementia. *Alzheimers Dement.* 2015;11(4):434-443.

(37) Silverberg GD, Mayo M, Saul T, Fellmann J, Carvalho J, McGuire D. Continuous CSF drainage in AD: Results of a double-blind, randomized, placebo-controlled study. *Neurol.* 2008;71(3):202-209.

(38) Sepulcre J, Schultz AP, Sabuncu M et al. In Vivo Tau, Amyloid, and Gray Matter Profiles in the Aging Brain. *J Neurosci.* 2016;36(28):7364.
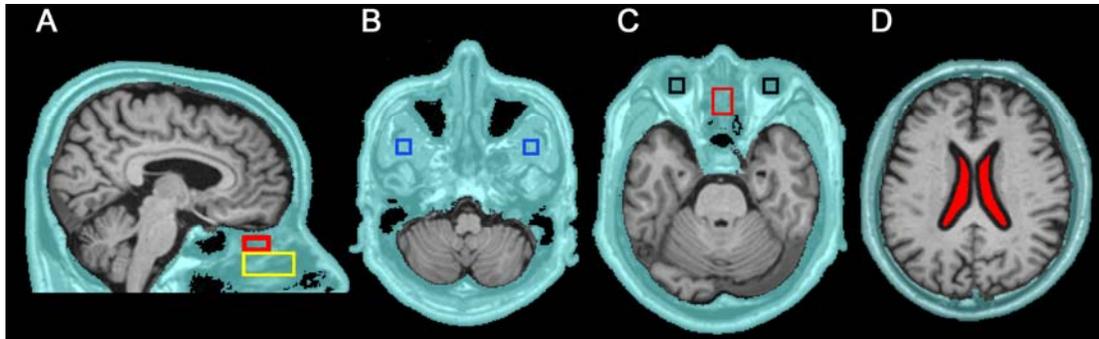
FIGURE. 1 The extra-cranial shell and regions of interest. The extra-cranial shell region (A-D) is in aqua. The following subregions were examined: A. the superior (red) and middle turbinates (yellow), B. pterygoid muscle (blue): C. globes of the eye (black) and superior turbinate (red); and D. the ventricular CSF (filled red).
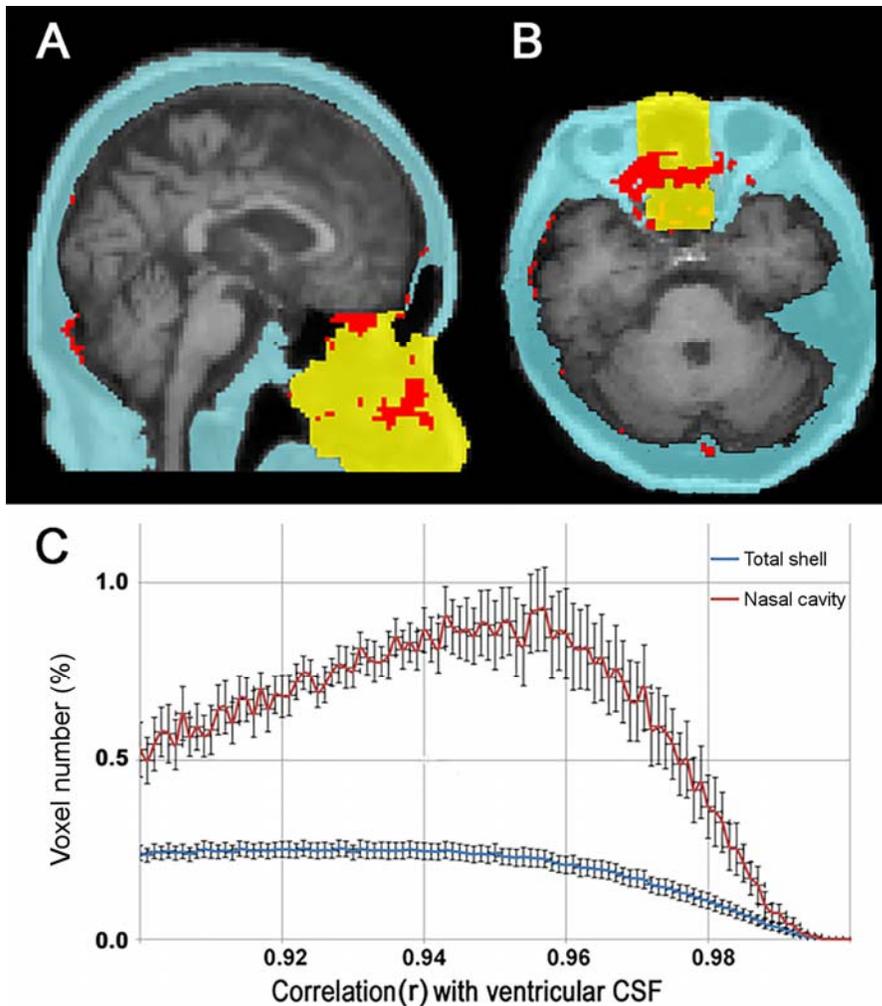
FIGURE 2. The extra-cranial distribution of CSF TAC correlated voxels.

Panel 2A (sagittal view) and 2B (axial view) MRI from a representative NL show the 3D extra-cranial shell region in blue and yellow (the total nasal cavity). 2C shows for 15 subjects, the percentage distribution (+/- SEM) of shell and nasal cavity voxels whose tau PET derived TAC are correlated with the ventricular CSF TAC, within the range of r= .90 to .99. The data show a 3 fold greater percentage of CSF correlated voxels in the nasal cavity than in the total shell. Shell voxels correlated at r>.95 were considered CSF positive and are mapped in red in Panels A and B.
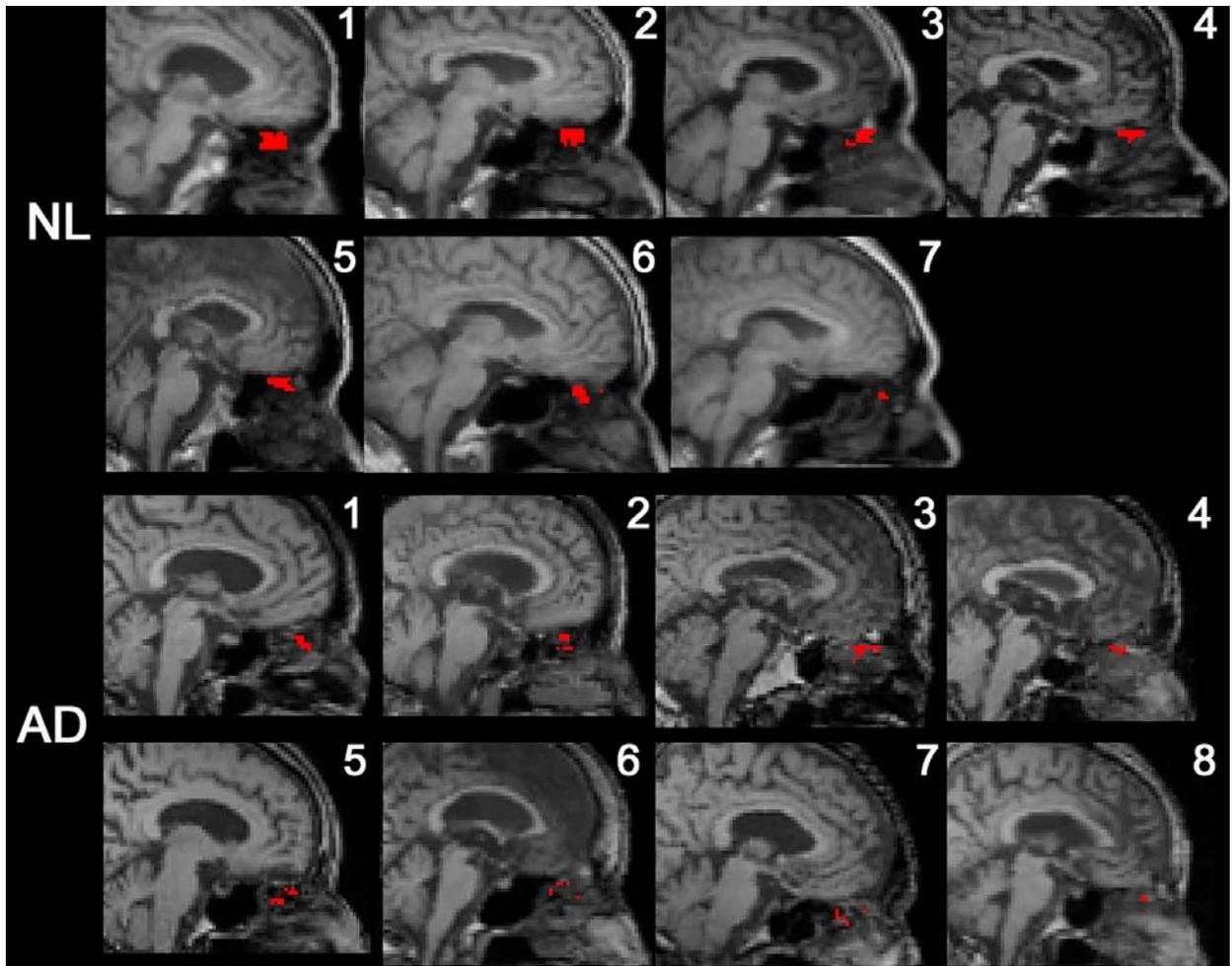
**FIGURE 3. Mid-sagittal MRI with superimposed PET data from all subjects.**

CSF positive voxels falling into the superior turbinate ROI are mapped in red.
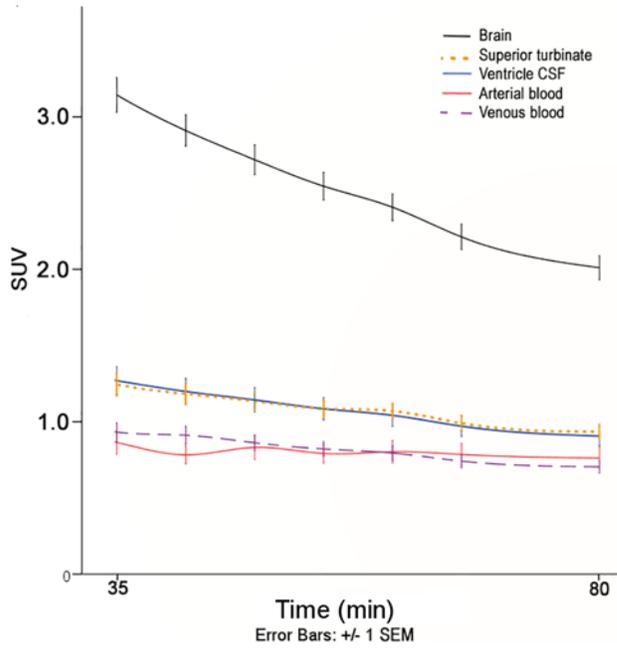
FIGURE 4. Tau tracer concentrations for 5 tissue types over time. The averaged tau tracer counts (SUV) +/- SEM for all study subjects plotted over 35-80min. Tracer concentrations from CSF positive superior turbinate and ventricular CSF do not differ from each other, but both are significantly different than blood and brain (p's<.05).
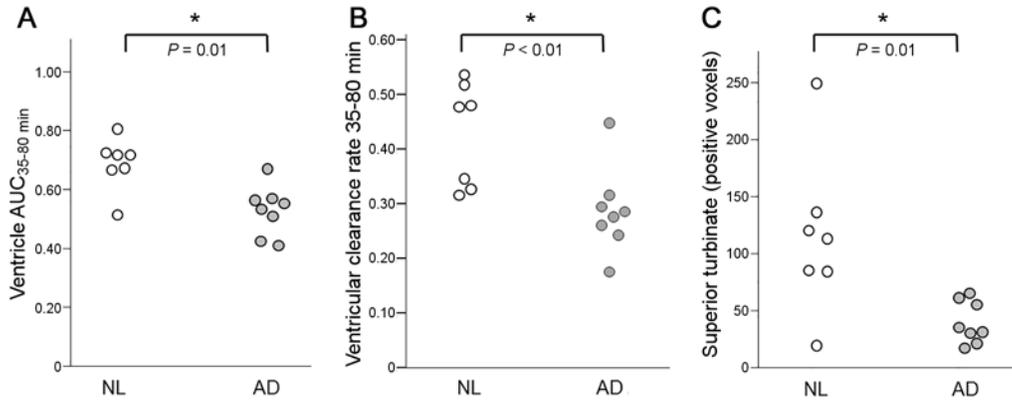
FIGURE 5A-C. Ventricle and superior turbinate CSF clearance in AD. As compared with NL, AD subjects show: (A) reduced magnitude of ventricular tracer ($AUC_{35-80min}$), (B) reduced rate of ventricular tracer clearance, and (C) a lower number of CSF positive superior turbinate voxels.
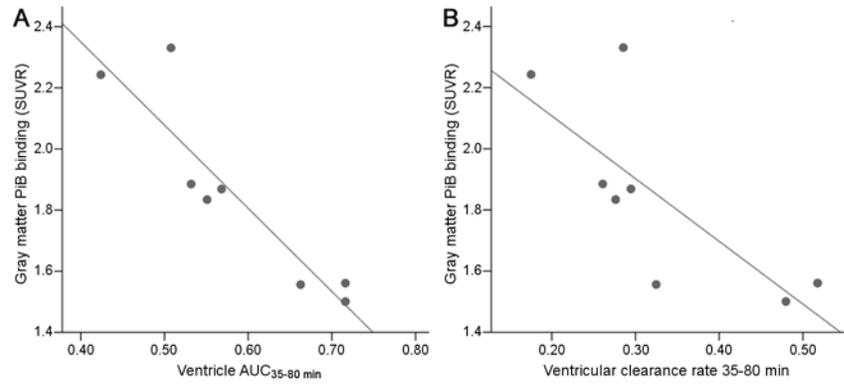
FIGURE. 6 A-B. Amyloid binding and CSF clearance. The relationship, for 8

PiB positive subjects, between the gray matter amyloid binding SUVR and (A)

the ventricular tracer AUC$_{35-80min}$, rho=.93, p<.01 and (B) the rate of ventricular

tracer clearance, rho=.74, p<.05.

Table 1: Study Subjects

Characteristic	NL n=7	AD n=8
Age (y) range	74.1 ± 5.6 (67-83)	79.8 ± 10.6 (57-89)
Education (y)	14.6 ± 2.2	12.1 ± 2.7
Male/female (n)	4/3	2/6
MMSE	28.7 ± 1.6	18.1 ± 4.6*
CDR	0.0± 0.0	2.0 ± 0.8*
Disease duration (y)	-	5.3±1.7

Values are mean ± sd, *$p<.05$

Table 2: Shell regions, n=15

	Superior turbinates	Middle turbinates	Eye	Muscle	Shell
Number Voxels in ROI	315	1160	360	216	181621 ± 23086
Number Positive Voxels	74.7± 61.7	264.9 ±194.4	15.4 ± 13.2	5.62 ± 5.08	7139.0 ± 3520.8
ROI Positive Voxel density%	23.7 ± 20.1	22.8 ±15.9	4.3 ± 3.6*	2.6 ± 2.3*	3.9 ± 2.0*
Tracer Concentration (mean SUV 35-80 min)	1.27 ± .25	1.12 ± .23*	0.71 ± .58*	0.86 ± .51*	1.09 ± .11*

Values are mean ± sd
* = different from superior turbinate, Wilcoxon Signed Rank Test $p<.02$

Supplemental Files

Supplemental File 1: lists the frame timing information of the reconstructed PET images

	THK-5117				PiB		
Frame number	duration (sec)	start time (min)	end time (min)	Frame number	scan duration (sec)	start time (min)	end (time)
1	10	0	0.2	1	10	0.0	0.2
2	10	0.2	0.3	2	10	0.2	0.3
3	10	0.3	0.5	3	10	0.3	0.5
4	10	0.5	0.7	4	10	0.5	0.7
5	10	0.7	0.8	5	10	0.7	0.8
6	10	0.8	1	6	10	0.8	1.0
7	10	1	1.2	7	20	1.0	1.3
8	10	1.2	1.3	8	20	1.3	1.7
9	10	1.3	1.5	9	20	1.7	2.0
10	10	1.5	1.7	10	60	2.0	3.0
11	10	1.7	1.8	11	60	3.0	4.0
12	10	1.8	2	12	180	4.0	7.0
13	60	2	3	13	180	7.0	10.0
14	60	3	4	14	300	10.0	15.0
15	120	4	6	15	300	15.0	20.0
16	240	6	10	16	300	20.0	25.0
17	300	10	15	17	300	25.0	30.0
18	300	15	20	18	300	30.0	35.0
19	300	20	25	19	300	35.0	40.0
20	300	25	30	20	300	40.0	45.0
21	300	30	35	21	300	45.0	50.0
22	300	35	40	22	300	50.0	55.0
23	300	40	45	23	300	55.0	60.0
24	300	45	50	24	300	60.0	65.0
25	300	50	55	25	300	65.0	70.0
26	300	55	60				
27	600	60	70				
28	600	70	80				

Supplemental File 2

For each subject, we identified and anatomically mapped CSF positive voxels in the shell region. For every shell voxel (v), a time activity curve (TAC) was correlated (Pearson Product r) with the TAC from the ventricular CSF. The correlations were derived from 14 time points spanning a 3-80 min interval. Formally, , if t_1, t_2, …. t_n are time points in a dynamic PET acquisition, $y_i = v\ (t_i)$ is the time activity curve of a shell voxel and $x_i = CSF\ (t_i)$ the time activity curve from CSF, and x and y bar indicate the average value we computed:

$$r = \frac{\sum x_i y_i - n\,\bar{x}\bar{y}}{\sqrt{(\sum x_i^2 - n\bar{x}^2)}\sqrt{(\sum y_i^2 - n\bar{y}^2)}}$$

The figure illustrates this concept on two sample time activity curves. Shell voxels correlated with ventricular CSF with r≥.95 were considered CSF positive.
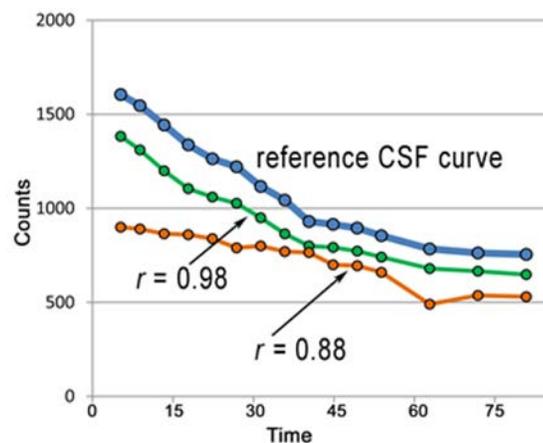
Supplemental File 2 (Supplemental Fig.1) schematic comparison of TAC curves. The figure shows a reference TAC for CSF (blue) and TAC for two sample shell voxels: green = voxel highly correlated with CSF, $r = .98$; and orange curve shows lower correlation $r = .88$. The correlations were based on the 3-80min time frames.

Supplemental File 3:

Supplemental Table 1: Partial volume corrections for tracer concentrations in Table 1

| SUV (35-80)	S. turbinate	M. turbinate	Eye	Muscle	Shell
	1.26 (.24)	1.12 (.23) *	.71 (.58) *	.83 (.50) *	1.06 (.11) *

Data show Mean SUV 35-80min (SD)
* = different from superior turbinate, Wilcoxon Signed Rank Test p<.01

Supplemental File 4:
Dynamic PET studies of 40 min duration were carried out with a CTI 931 tomograph after injection of 6–8 mCi of ^{11}C-cocaine. Prior work has shown that there is rapid clearance and weak cortical binding of the tracer. We observed there was no nasal turbinate binding of the tracer in the 4 subjects studied.
The correlation between the ventricle sample ("peeled" 2 voxels around the ventricular margins) and all shell voxels was conducted as described in the text. To avoid partial volume errors, this procedure requires a relatively large ventricle to obtain a CSF sample. The study was limited to the older subjects who typically have larger ventricles.

1. Volkow ND, Wang G, Fischman MW, Foltin R, Fowler JS, Franceschi D, Franceschi M, Logan J, Gatley SJ,W ong C, Ding YS, Hitzemann R, Pappas N (2000) Effects of route of administration on cocaine induced dopamine transporter blockade in the human brain. Life Sci 67: 1507-1515.
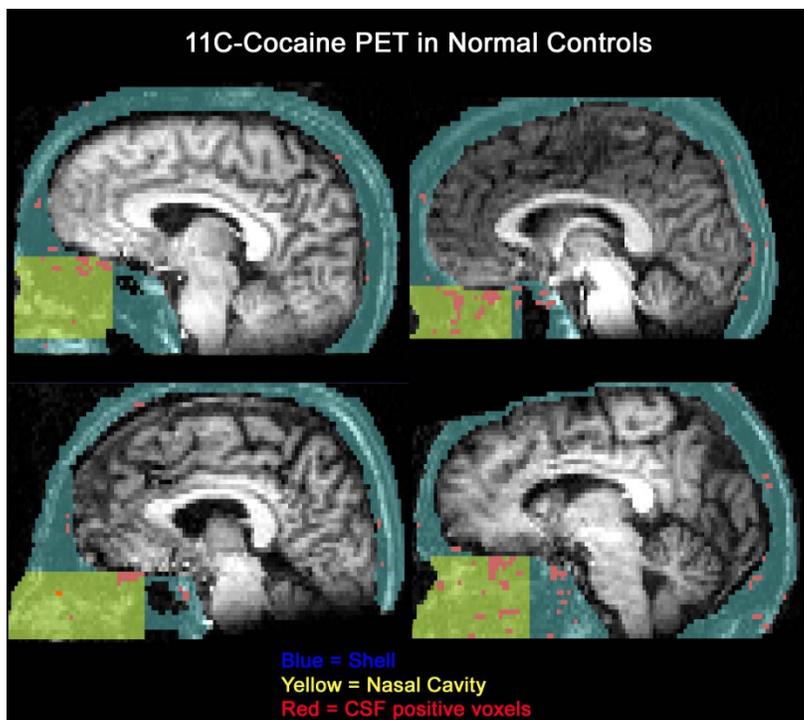
Supplemental File 4 (Supplemental Fig.2) Voxels whose correlations exceeded r=.95 were considered CSF positive and are mapped in red below. Within the blue shell region, a nasal cavity

region was defined in yellow. As observed with the THK5117 tau tracer, the highest density of presumed CSF positive sites is in the superior and middle turbinate regions.

Supplemental 5 Video: Normal Subject Clearance

The ventricular CSF correlated nasal turbinate voxels are well seen in the video which visualizes the extra-cranial CSF transit over 9 min. Video 1 is a normal control subject demonstrating the transit of CSF correlated turbinate voxels from superior to inferior levels. Significant correlations first appear 3min post injection, at the superior turbinate and peri-dural areas and later are found more diffusely in the middle and inferior turbinates.

The video uses progressive 1 min temporal offsets for the correlations between the ventricle TAC and the TAC for individual shell voxels to demonstrate the anatomical trajectory of highly correlated CSF voxels. This was done by offsetting in 1 min increments the shell TAC and recomputing the correlation maps. With the ventricular TAC fixed at 3min post-injection, for example for 1 min delay, the shell TAC would start at 4min post-injection. For data delayed by 2 min, shell voxels acquired after 5min were aligned with the 3 min ventricular TAC, etc. We visualized for 9 minutes of offset the spatio-temporal trajectory of the CSF signal through the shell.

Supplemental File 6 The relationship between the ventricular clearance of THK5117 and PiB
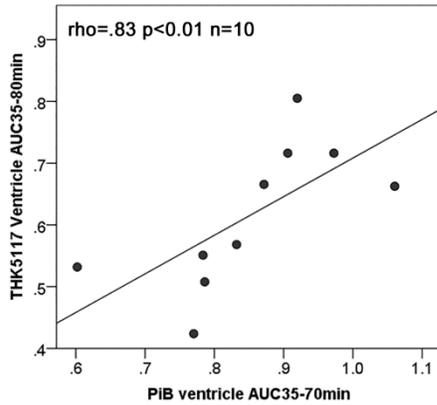
Supplemental File 6 (Supplemental Fig.3). Demonstrates the relationship between the ventricular clearance of THK5117 and PiB on the same subjects. For 10 subjects with both THK5117 and PiB scans we examined the correlation between the ventricular AUC35-80min. These data (rho=.83, p<.01) highlight the excellent precision of the ventricular CSF clearance measure.

Supplemental 7. The relationship between tau binding and CSF clearance.
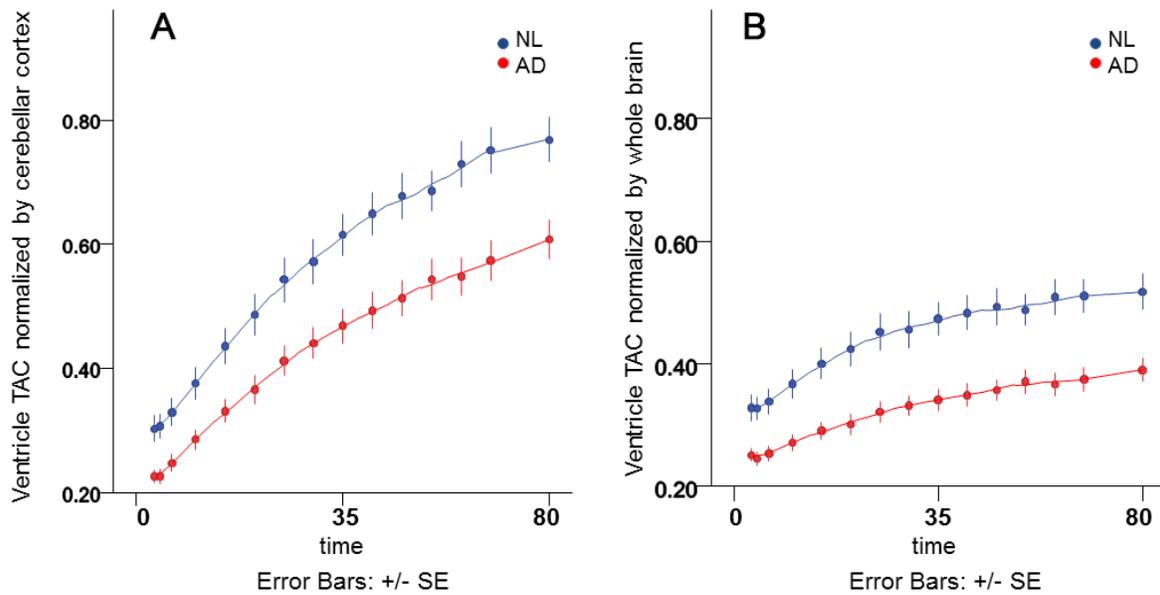
Supplemental file 7 (Supplemental Fig.4). Compared with NL, AD subjects show lower ventricular AUC$_{35-80min}$ with both (A) cerebellar gray matter normalization (p=.01) and (B) total brain parenchyma normalization (p<.01).These data suggest large between group clearance differences with relatively smaller differential contributions from overall tracer retention.

Supplemental File 8: Simulating cerebral blood flow (CBF) effects on the area under curve.
One possible explanation for regional differences in area under the curve (AUC) is the CBF. To estimate the effect of regional perfusion rate F on AUC, representative datasets were simulated for a wide range of F. The simulation was governed by the kinetic model of a diffusible tracer in which the relation between the arterial input function c_a (t) and the tissue response function c (t) is given by:

$$c'(t) = F\{c_a(t) - c(t)\} \qquad \text{Eq. 1}$$

where prime denotes the time derivative. The analytic solution of Eq.1 is:

$$c(t) = Fe^{-Ft} \int_0^t c_a(u)e^{Fu}\,du \qquad \text{Eq. 2}$$

The arterial input was generated as the average of values extracted from all 15 patients after aligning the peaks..
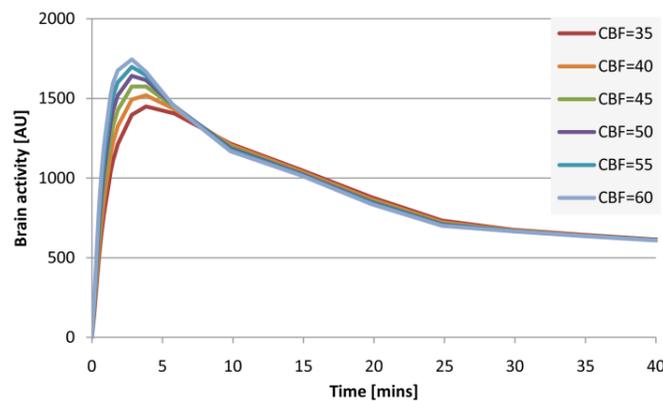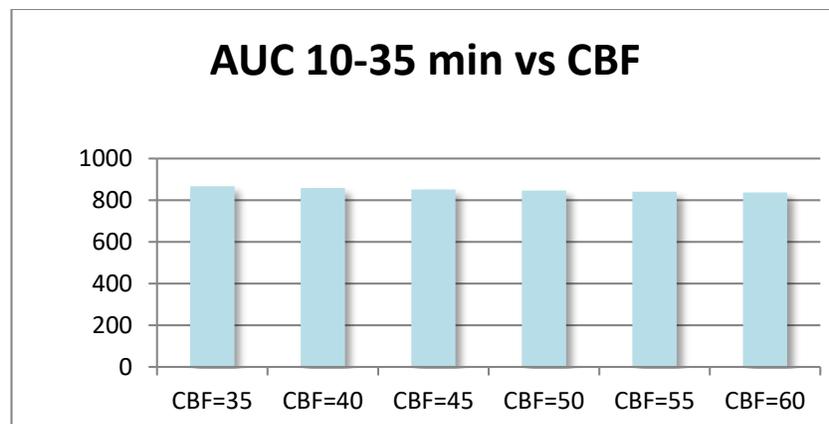
Fig. A

Fig. B

Supplemental file 8 (Supplemental Fig.5) A-B. **5A** shows the tissue activity curves for F varying in the range 35-60 ml/100g/min. **5B.** shows the corresponding distribution of AUC for the time period 10-35 min after injection, demonstrating negligible effect of F. These data show that the AUC were not affected by CBF over the time ranges studied.